Electrochemical Water Splitting | Hot Paper

Deutsche Ausgabe: DOI: 10.1002/ange.201607405
Internationale Ausgabe: DOI: 10.1002/anie.201607405

Nitrogen, Phosphorus, and Fluorine Tri-doped Graphene as a Multifunctional Catalyst for Self-Powered Electrochemical Water Splitting

*Jintao Zhang and Liming Dai**

Abstract: *Electrocatalysts are required for clean energy technologies (for example, water-splitting and metal-air batteries). The development of a multifunctional electrocatalyst composed of nitrogen, phosphorus, and fluorine tri-doped graphene is reported, which was obtained by thermal activation of a mixture of polyaniline-coated graphene oxide and ammonium hexafluorophosphate (AHF). It was found that thermal decomposition of AHF provides nitrogen, phosphorus, and fluorine sources for tri-doping with N, P, and F, and simultaneously facilitates template-free formation of porous structures as a result of thermal gas evolution. The resultant N, P, and F tri-doped graphene exhibited excellent electrocatalytic activities for the oxygen reduction reaction (ORR), oxygen evolution reaction (OER), and hydrogen evolution reaction (HER). The trifunctional metal-free catalyst was further used as an OER–HER bifunctional catalyst for oxygen and hydrogen gas production in an electrochemical water-splitting unit, which was powered by an integrated Zn–air battery based on an air electrode made from the same electrocatalyst for ORR. The integrated unit, fabricated from the newly developed N, P, and F tri-doped graphene multifunctional metal-free catalyst, can operate in ambient air with a high gas production rate of 0.496 and 0.254 $\mu L s^{-1}$ for hydrogen and oxygen gas, respectively, showing great potential for practical applications.*

The oxygen evolution reaction (OER) and hydrogen evolution reaction (HER) are crucial for generation of oxygen and hydrogen gases by electrochemical water splitting; these reactions may be considered green and renewable sources of energy.[1] Similarly, the oxygen reduction reaction (ORR) is also important to renewable energy technologies, including fuel cells and metal-air batteries.[2] To make these reactions viable, however, electrocatalysts are required to lower their overpotentials and thereby speed up the reaction rates.[3] Pt-based catalysts have long been used as efficient electrocatalysts for ORR and HER, but their catalytic activities towards OER are relatively poor. On the other hand, metal oxides (such as, RuO_2, IrO_2, and perovskite oxides) have been widely studied as electrocatalysts for OER,[4] while their catalytic activities for HER need to be further improved. Therefore, finding electrocatalysts that can work efficiently for ORR, OER, and HER has been amongst the "holy grails" of chemistry for decades.[3a] Even when realized, the high-cost, low-reserve, and poor durability of metal-based multifunctional catalysts could still prevent them from practical applications in renewable energy technologies.

Heteroatom-doping of carbon nanomaterials has recently been demonstrated to impart electrocatalytic activities to carbon-based metal-free catalysts.[3,5] Since the discovery that vertically aligned N-doped carbon nanotubes (VA-NCNTs) can act as efficient metal-free electrocatalysts for ORR in alkaline electrolytes with a four-electron pathway and free from methanol cross-over and CO-poisoning effects,[6] tremendous progress has been made and a large number of metal-free catalysts have been reported by doping of various graphitic carbon materials (for example, CNTs, graphene, and graphite) with nitrogen and/or many other heteroatoms (for example, B, S, and P).[3,7] Of particular interest, co-doping of graphitic carbon atoms with two heteroatoms (such as, N or B), of different electronegativities from that of C, was found to further enhance the electrocatalytic activity by a synergic effect with respect to single heteroatom-doped counterparts.[7–8] Interestingly, we have recently further demonstrated that ORR–OER and ORR–HER bifunctional catalysts (useful for metal-air batteries and regenerative fuel cells, respectively) can be produced by co-doping of different three-dimensional carbon assemblies with N and P.[9] However, it is still challenging to develop triple functional metal-free electrocatalysts for ORR, OER, and HER. If realized, cost-effective integrated self-powered water-splitting units could be devised to produce hydrogen and oxygen gases for renewable energy technologies.

Herein, we report a facile route to N, P, and F tri-doped graphene metal-free electrocatalysts for ORR, OER, and HER, by pyrolysis of polyaniline (PANi)-coated graphene oxide (GO-PANi) in the presence of ammonium hexafluorophosphate (AHF). Thermal decomposition of AHF could, not only provide heteroatom sources for tri-doping with N, P, and F, but also facilitate the template-free formation of porous structures by thermal gas evolution. The resultant N, P, and F tri-doped graphene was demonstrated to exhibit excellent electrocatalytic activities for ORR, OER, and HER. We further used this newly developed trifunctional metal-free catalyst as an OER–HER bifunctional catalyst for oxygen and hydrogen gas production in an electrochemical water-splitting unit, which was powered by an integrated

---

[*] Dr. J. Zhang, Prof. L. Dai
Center of Advanced Science and Engineering for Carbon (Case4-carbon), Department of Macromolecular Science and Engineering
Case Western Reserve University
10900 Euclid Avenue, Cleveland, OH 44106 (USA)
E-mail: liming.dai@case.edu

Dr. J. Zhang
Key Laboratory of Colloid and Interface Chemistry
Shandong University (China)

Supporting information for this article can be found under: http://dx.doi.org/10.1002/anie.201607405.

Zn–air battery based on an air electrode made from the same electrocatalyst for ORR. This first self-powered integrated water-splitting unit, based on the tri-functional metal-free carbon catalyst, can operate in ambient air with a high gas production rate of 0.496 and 0.254 $\mu L\,s^{-1}$ for hydrogen and oxygen gas, respectively, showing great potential for practical applications.

PANi was first deposited on the surface of GO by an oxidative polymerization method (Scheme 1). The obtained GO-PANi was activated with AHF by thermal treatment (Supporting Information). The pyrolysis of polyaniline and the thermal decomposition of AHF resulted in formation of reduced graphene oxide doped with nitrogen, phosphorous, and fluorine (designated as GO-PANi-FP).

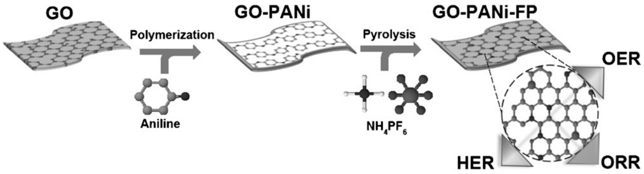

Scheme 1. The preparative process for GO-PANi-FP tri-functional electrocatalyst.

As shown in Figure 1 A, GO-PANi is composed of interconnected thick layers as a result of the surface coating of GO with a PANi layer. After the thermal treatment, similar morphologies were observed for GO-PANi31-FP (Figure 1 B) and GO-PANi51-FP (Figure 1 C)—here, 31 and 51 refer to the initial mass ratio of GO-PANi and ammonium hexafluorophosphate as 3:1 and 5:1, respectively, annealed at 950 °C for 1 h (Supporting Information). The TEM image in Figure 1 D reveals the wrinkled structure of the GO-PANi31-FP sheet, suggesting the thin layered nature of the carbonized PANi and GO composite sheet.[10] To examine the distribution of heteroatoms, we performed elemental mapping analysis. As seen in Figure 1 E, a uniform distribution of C, N, P, and F was evident, indicating homogeneous doping of graphene sheets with N, P, and F. The heteroatom-doping could change the surface properties of and introduce defects into graphene sheets, and hence improve electrocatalytic activity.[9a,11]

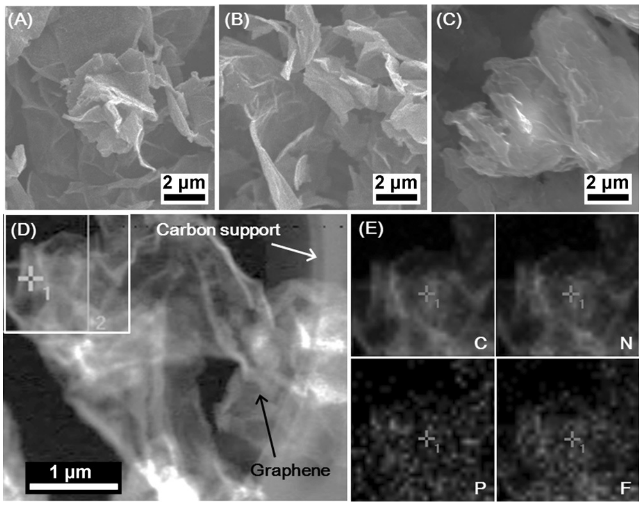

Figure 1. SEM images of A) GO-PANi, B) GO-PANi31-FP, and C) GO-PANi51-FP. TEM images of D) GO-PANi31-FP and the corresponding E) elemental mappings of C, N, P, and F.

The X-ray diffraction (XRD) patterns of GO-PANi before and after the thermal treatment were recorded. For GO-PANi, Figure S1 (Supporting Information) shows typical XRD peaks attributable to the partially crystallized PANi coated on graphene oxide.[9a] After the thermal treatment, only a broad diffraction peak at around 26° was observed for GO-PANi31-FP and GO-PANi51-FP, suggesting conversion of PANi into graphitic carbon. It is worth noting that the thermal decomposition of AHF can provide nitrogen, phosphorus, and fluorine sources for tri-doping of graphene sheets with N, P, and F, while thermal gas evolution can facilitate a template-free formation of porous structures. Fourier transform infrared spectroscopy (FTIR) was performed to examine the changes of surface functional groups. For GO-PANi, Figure S2 (Supporting Information) shows the characteristic bands at 1584 and 1484 cm^{-1} arising from the C=C stretching vibration in quinoid and benzene rings, respectively, whereas the bands at 1295 and 1240 cm^{-1} were attributed to the C–N and C=N stretching modes of polyaniline.[12] The presence of these bands suggested the successful coating of PANi on GO sheets. After thermal treatment, the functional groups of GO-PANi disappeared (Supporting Information, Figure S2), suggesting a successful thermal conversion of the PANi functionalized GO into the heteroatom-doped graphene.

To investigate the chemical composition, we further performed X-ray photoelectron spectroscopy (XPS) measurements. As expected, the XPS survey spectrum of GO-PANi31-FP shows peaks for C, N, P, F, and O (Figure 2 A), indicating the tri-doping of carbon with N, P, and F. The presence of an O 1s peak possibly arises from the oxygen-containing groups derived from the GO (see below) or the incoporation of physicochemically adsorbed oxygen.[13] Figure 2 B and Figure S3 (Supporting Information) show the core-level XPS spectra for GO-PANi31-FP, GO-PANi51-FP, and GO-PANi-950. Table S1 (Supporting Information) lists the contents of N, P, and F for all samples. As can be seen, the XPS N 1s spectrum was fitted to four component peaks centred at about 398.7, 400.5, 401.4, and 402.9 eV, attributable to pyridinic, pyrrolic, graphitic, and oxidized nitrogen, respectively.[14] The pyridinic and graphitic N species are dominant, which could enhance electrocatalytic activities.[15] In the XPS P 2p spectrum, the P–C bond is located at about 132.2 eV, while the component peak at around 133.6 eV suggests the presence of a P–O bond. The high-resolution XPS F 1s spectrum for GO-PANi31-FP exhibits ionic (684.9 eV) and semi-ionic (687. 8 eV) C–F bonds. Heteroatom-doping changed the surface charge/defect distributions of the carbon matrix, leading to advanced electrocatalytic activities.[6b,8b] Having a high electronegativity,[3b] F is a highly promising heteroatom dopant to induce strong charge redistribution along with possible changes in surface hydrophobicity, and hence significantly enhanced catalytic activities for graphitic-carbon atoms, even after co-doping.

Raman spectra of GO-PANi31-FP and GO-PANi51-FP, given in Figure 2 C, clearly show the D- and G-bands,

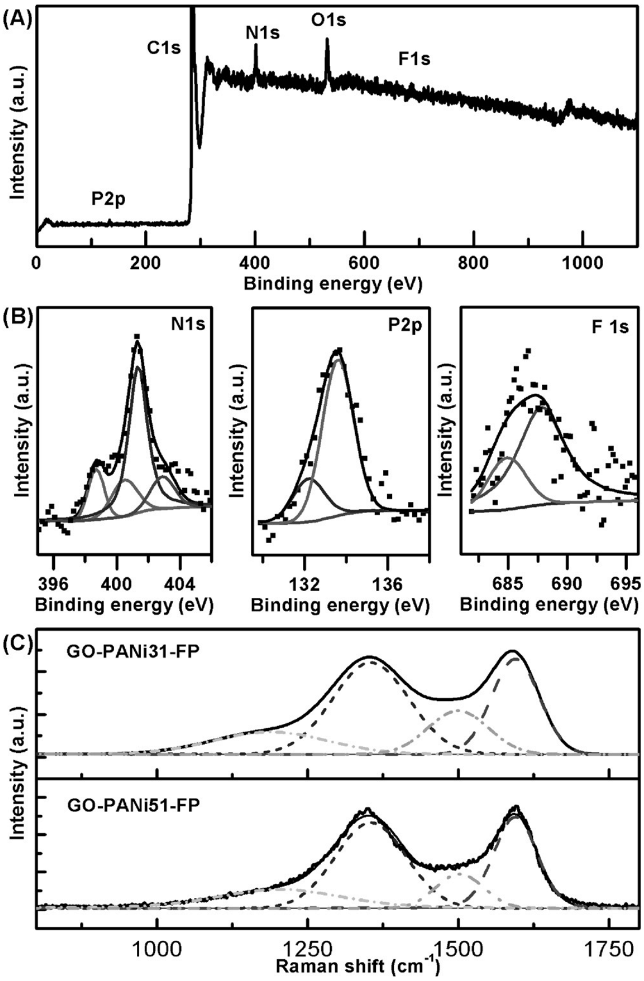

Figure 2. Survey XPS of A) GO-PANi31-FP and B) core level XPS of N 1s, P 2p, and F 1s. C) Raman spectra of GO-PANi31-FP and GO-PANi51-FP.

suggesting that the PANi in GO-PANi samples have been successfully transformed into graphitic carbon atoms.[16] Furthermore, these Raman peaks can be deconvoluted into a series of four component peaks, centered at around 1200, 1355, 1500, and 1600 cm^{-1}. The characteristic peaks at around 1355 cm^{-1} (D-band) and 1600 cm^{-1} (G-band) are associated with the defects in the graphene structure, including those carbon atoms near to the edge of a graphene sheet, and the planar motion of sp^2-hybridized carbon atoms in a graphene layer, respectively. The broad band at about 1200 cm^{-1} arises from carbon atoms outside a perfectly planar graphene network (such as, aliphatic and amorphous structures). The peak at approximately 1500 cm^{-1} is due to the distorted structures caused by the incorporation of five-membered rings or heteroatoms in the graphene hexagonal network,[17] indicating the occurrence of doping of heteroatoms into the carbon matrix, thereby imparting electrocatalytic activity.[3,6] The N_2 adsorption–desorption isotherm curves (Supporting Information, Figure S4) for the GO-PANi31-FP, GO-PANi51-FP, and GO-PANi-950, exhibit an increase in absorbed volumes with increasing AHF content. The specific surface areas for GO-PANi31-FP and GO-PANi51-FP are 512 and 415 m^2 g^{-1}, which are larger than that of GO-PANi-950 (218 m^2 g^{-1}). Furthermore, the pore size distribution curves (Supporting Information, Figure S4b) reveal an increase in mesopore population with increasing AHF content. These results suggest that AHF is responsible for the formation of the porous structure by thermal release of gas, which serves as a soft template.

To demonstrate the electrochemical catalytic activities of GO-PANi-FP samples, we carried out linear scan voltammetry (LSV) measurements with a rotating ring-disk electrode (RRDE). Figure S5 (Supporting Information) shows increases in the reduction currents with increasing rotating speed, suggesting diffusion controlled oxygen reduction in alkaline electrolyte.[10,18] GO-PANi31-FP exhibited the strongest and most stable limiting current density because of its efficient catalytic activity arising from synergic effects of the tri-doping with a balanced composition of heteroatoms.[8,19] Figure 3 A shows the corresponding RRDE results for the GO-PANi-950 and GO-PANi-FP samples. Once again, GO-PANi31-FP exhibited the best catalytic activity with the highest onset potential and strongest limiting current density, though its half-wave potential is still 40 mV lower than that of a Pt/C electrode. The calculated number of electrons transferred at the GO-PANi31-FP electrode is around 3.85 (Figure 3B and Equation (1) in the Supporting Information), indicating a four-electron pathway for the oxygen reduction.[20] The observed good ORR catalytic activity of the GO-PANi31-FP electrode was also confirmed by the low percentage ($<10\,\%$) of H_2O^- generated during the oxygen reduction (Figure 3C).

Figure 3D also shows the heteroatom-doping enhanced OER catalytic activities for GO-PANi-FP samples. The onset potential for OER at the GO-PANi31-FP electrode is around 1.62 V, which is higher than that of a RuO_2 catalyst (ca. 1.53 V). Nevertheless, the overpotentials at a current density of 10 mA cm^{-2} for both GO-PANi31-FP and RuO_2 catalysts are similar (Figure 3D). Compared with GO-PANi-950 and GO-PANi51-FP, GO-PANi31-FP exhibited the best OER performance with the largest current density and lowest onset potential. The corresponding Tafel plots are given in Figure 3E, which shows the lowest slope (136 mV dec^{-1}) for GO-PANi31-FP—comparable to that of RuO_2 catalyst (141 mV dec^{-1}) and much lower than those of GO-PANi51-FP (238 mV dec^{-1}) and GO-PANi-950 (221 mV dec^{-1}). These results clearly show that GO-PANi31-FP is also the best metal-free OER catalyst. Furthermore, the polarization curves and corresponding Tafel plots (Figure 3F and Figure 3G, respectively) show reasonably good HER catalytic activities for GO-PANi31-FP, with an onset potential of about −0.4 V. The corresponding overpotential at a current density of 10 mA cm^{-2} is around 0.52 V, which is still poorer than that of Pt/C (ca. 0.19 V) in an alkaline electrolyte. Additionally, GO-PANi31-FP electrode exhibited an excellent stability for OER and ORR/HER with respect to RuO_2 and Pt/C, respectively (Supporting Information, Figure S6).

The good tri-functional electrocatalytic activities of GO-PANi31-FP observed in ORR, OER, and HER, prompted us to construct an integrated water-splitting unit.

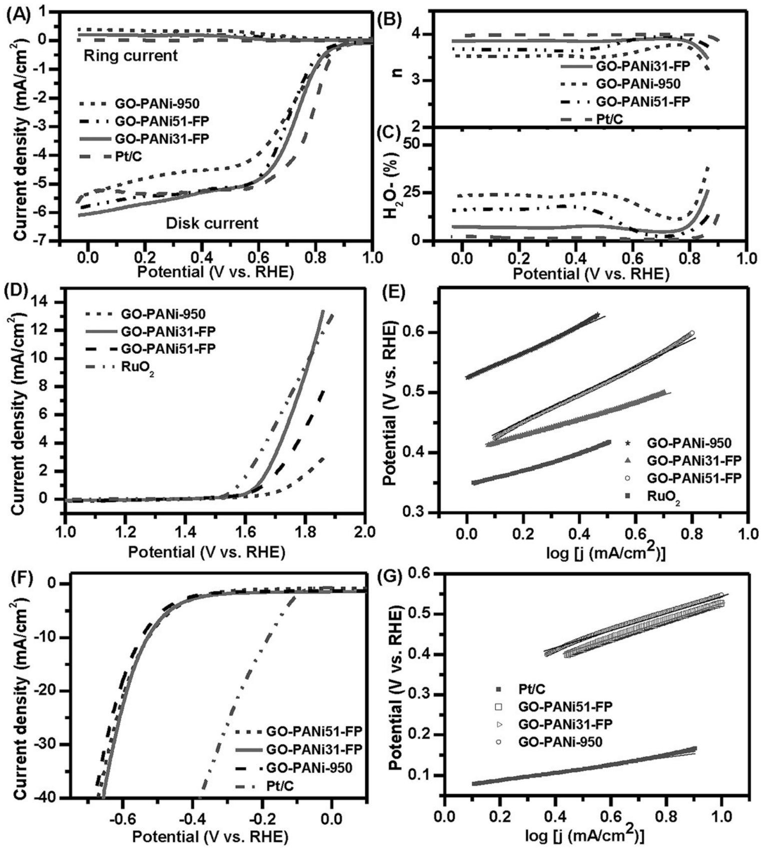

Figure 3. A) RRDE results of various catalysts for ORR; B) the number of electron transfer; C) the percentage of peroxide in the total oxygen reduction products for ORR, based on the RRDE results in (A). D) LSV curves of various samples for OER in 0.1 M KOH and E) the corresponding Tafel curves. F) LSV curves for HER and G) the corresponding Tafel curves.

The unit was powered by a Zn–air battery based on the newly developed metal-free tri-functional carbon catalyst for ORR, as well as OER and HER in the water-splitting process. Figure S7 (Supporting Information) shows a high power density of around 38 mW cm^{-2} and good stability (no obvious potential decay over 50 h) for Zn–air batteries based on the GO-PANi31-FP air cathodes.

For electrochemical water splitting, the following reactions lead to oxygen (Reaction (1)) and hydrogen (Reaction (2)) generation at the anode and cathode, respectively.

$$4\,OH^- \rightarrow 2\,H_2O + O_2 + 4\,e^- \quad (1)$$

$$4\,H^+ + 4\,e^- \rightarrow 2\,H_2 \quad (2)$$

However, electrocatalysts are often required to lower the energy barrier and improve the efficiency of these reactions.[21] To demonstrate the multifunctional applications of our newly developed tri-functional electrocatalysts, we connected the above-mentioned Zn–air battery to a water-splitting unit, in which GO-PANi31-FP-coated nickel foams were used as electrodes for both O_2 and H_2 generation (Supporting Information, Figure S8). Figures 4 A and 4 B exhibit continuous generation of gas bubbles (see, Movie S1 in the Supporting Information) on the two electrodes in the integrated device, consisting of the GO-PANi31-FP-based water-splitting unit and Zn–air battery.

To collect gasses produced during the self-powered water-splitting process, we inserted the anode and cathode into tubes with volume marks and then sealed the top end of the tubes with epoxy (Supporting Information, Figure S9). Initially, each tube containing one electrode was filled with KOH electrolyte and its bottom end immersed into the electrolyte in a beaker (Supporting Information, Figure S9A). When the water-splitting unit was connected to the Zn–air battery, the gases produced (H_2 and O_2) were collected on the top of the water filled tubes. Meanwhile, the water surface level inside the tube dropped down because the electrolyte gradually flowed out of the bottom ends of the immersed tubes as the internal gas pressure on the top of the tubes built up during the water-splitting process; in this way the gas volume produced was recorded. As demonstrated in Figure S9B (Supporting Information), the electrolyte surface level within the tube gradually dropped down while the inside gas volume increased with increasing water-splitting time. It is worth noting that the increased gas volumes for hydrogen and oxygen are different. The recorded gas volumes as a function of the water-splitting time are given in Figure 4C, showing a linear relationship with a slope of 0.496 and 0.254 μL s^{-1} for hydrogen and oxygen gas, respectively. The slop ratio of 1.95 is very close to the theoretical ratio of two, as anticipated for hydrogen and oxygen production by water splitting.

In summary, we have demonstrated that thermal pyrolysis of polyaniline pre-coated graphene oxide in the presence of AHF, generated graphene materials tri-doped with nitrogen, phosphorus, and fluorine. The tri-doped graphene can be used as an efficient tri-functional electrocatalyst for ORR, OER, and HER. The newly developed tri-functional metal-free catalyst was further used as an OER–HER bifunctional catalyst for oxygen and hydrogen gas production in an electrochemical water-splitting unit, which was powered by a Zn–air battery based on an air electrode made from the same electrocatalyst for ORR. This integrated self-powered water-splitting unit can operate in ambient air with a high gas production rate of 0.496 and 0.254 μL s^{-1} for hydrogen and oxygen gas, respectively, showing great potential for practical applications. Therefore, the low-cost metal-free tri-functional electrocatalysts thus produced hold great promise for a wide range of applications.

Acknowledgements

This work was supported by the NSF (CMMI-1400274, CMMI-1266295, DMR 1106160).

Keywords: hydrogen evolution · oxygen evolution · oxygen reduction · water splitting · zinc–air battery

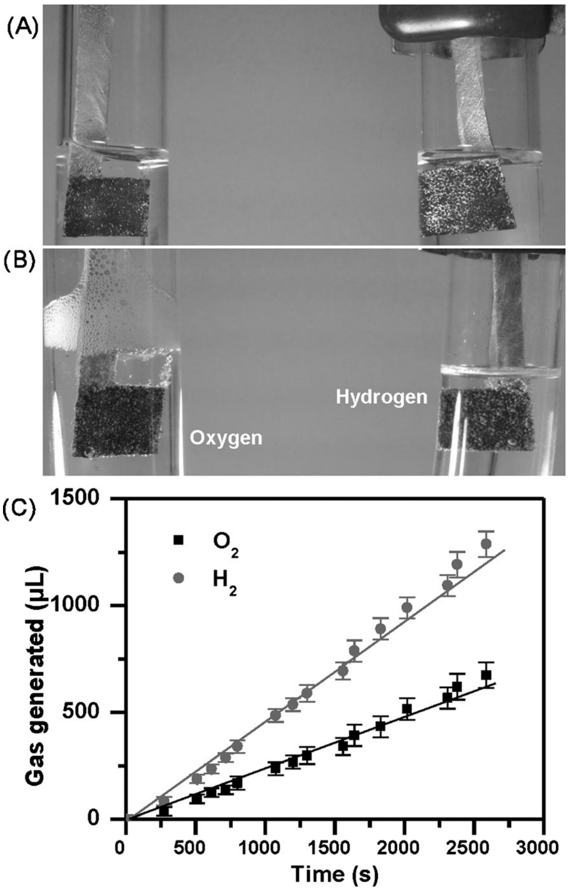

Figure 4. The optical images of electrodes A) before and B) after water splitting powered by Zn–air batteries. C) O_2 and H_2 production volumes as a function of water-splitting time.

How to cite: *Angew. Chem. Int. Ed.* **2016**, *55*, 13296–13300
Angew. Chem. **2016**, *128*, 13490–13494

---

[1] a) Y. Zheng, Y. Jiao, L. H. Li, T. Xing, Y. Chen, M. Jaroniec, S. Z. Qiao, *ACS Nano* **2014**, *8*, 5290–5296; b) G.-L. Tian, M.-Q. Zhao, D. Yu, X.-Y. Kong, J.-Q. Huang, Q. Zhang, F. Wei, *Small* **2014**, *10*, 2251–2259.

[2] a) Y. Li, W. Zhou, H. Wang, L. Xie, Y. Liang, F. Wei, J.-C. Idrobo, S. J. Pennycook, H. Dai, *Nat. Nanotechnol.* **2012**, *7*, 394–400; b) I. Katsounaros, S. Cherevko, A. R. Zeradjanin, K. J. J. Mayrhofer, *Angew. Chem. Int. Ed.* **2014**, *53*, 102–121; *Angew. Chem.* **2014**, *126*, 104–124.

[3] a) R. Li, Z. Wei, X. Gou, *ACS Catal.* **2015**, *5*, 4133–4142; b) J. Zhang, L. Dai, *ACS Catal.* **2015**, *5*, 7244–7253; c) L. Dai, Y. Xue, L. Qu, H.-J. Choi, J.-B. Baek, *Chem. Rev.* **2015**, *115*, 4823–4892.

[4] J. Suntivich, K. J. May, H. A. Gasteiger, J. B. Goodenough, Y. Shao-Horn, *Science* **2011**, *334*, 1383–1385.

[5] M.-M. Titirici, R. J. White, N. Brun, V. L. Budarin, D. S. Su, F. del Monte, J. H. Clark, M. J. MacLachlan, *Chem. Soc. Rev.* **2015**, *44*, 250–290.

[6] a) L. Dai, D. W. Chang, J.-B. Baek, W. Lu, *Small* **2012**, *8*, 1130–1166; b) K. Gong, F. Du, Z. Xia, M. Durstock, L. Dai, *Science* **2009**, *323*, 760–764.

[7] a) S. Wang, L. Zhang, Z. Xia, A. Roy, D. W. Chang, J. B. Baek, L. Dai, *Angew. Chem. Int. Ed.* **2012**, *51*, 4209–4212; *Angew. Chem.* **2012**, *124*, 4285–4288; b) W. Wei, H. Liang, K. Parvez, X. Zhuang, X. Feng, K. Müllen, *Angew. Chem. Int. Ed.* **2014**, *53*, 1570–1574; *Angew. Chem.* **2014**, *126*, 1596–1600; c) Z. Xiang, D. Cao, L. Huang, J. Shui, M. Wang, L. Dai, *Adv. Mater.* **2014**, *26*, 3315–3320.

[8] a) L. Qu, Y. Liu, J.-B. Baek, L. Dai, *ACS Nano* **2010**, *4*, 1321–1326; b) S. Wang, E. Iyyamperumal, A. Roy, Y. Xue, D. Yu, L. Dai, *Angew. Chem. Int. Ed.* **2011**, *50*, 11756–11760; *Angew. Chem.* **2011**, *123*, 11960–11964.

[9] a) J. Zhang, Z. Zhao, Z. Xia, L. Dai, *Nat. Nanotechnol.* **2015**, *10*, 444–452; b) J. Zhang, L. Qu, G. Shi, J. Liu, J. Chen, L. Dai, *Angew. Chem. Int. Ed.* **2016**, *55*, 2230–2234; *Angew. Chem.* **2016**, *128*, 2270–2274; c) Z. Zhao, M. Li, L. Zhang, L. Dai, Z. Xia, *Adv. Mater.* **2015**, *27*, 6834–6840.

[10] L. Lai, J. R. Potts, D. Zhan, L. Wang, C. K. Poh, C. Tang, H. Gong, Z. Shen, J. Lin, R. S. Ruoff, *Energy Environ. Sci.* **2012**, *5*, 7936–7942.

[11] N. Daems, X. Sheng, I. F. J. Vankelecom, P. P. Pescarmona, *J. Mater. Chem. A* **2014**, *2*, 4085–4110.

[12] C.-C. Hu, J.-Y. Lin, *Electrochim. Acta* **2002**, *47*, 4055–4067.

[13] P. G. Collins, K. Bradley, M. Ishigami, A. Zettl, *Science* **2000**, *287*, 1801–1804.

[14] S. Yang, L. Zhi, K. Tang, X. Feng, J. Maier, K. Müllen, *Adv. Funct. Mater.* **2012**, *22*, 3634–3640.

[15] D. Guo, R. Shibuya, C. Akiba, S. Saji, T. Kondo, J. Nakamura, *Science* **2016**, *351*, 361–365.

[16] a) I. Y. Jeon, H. J. Choi, M. J. Ju, I. T. Choi, K. Lim, J. Ko, H. K. Kim, J. C. Kim, J. J. Lee, D. Shin, S. M. Jung, J. M. Seo, M. J. Kim, N. Park, L. Dai, J. B. Baek, *Sci. Rep.* **2013**, *3*, 2260; b) X. Sun, P. Song, Y. Zhang, C. Liu, W. Xu, W. Xing, *Sci. Rep.* **2013**, *3*, 2505; c) I.-Y. Jeon, H.-J. Choi, M. Choi, J.-M. Seo, S.-M. Jung, M.-J. Kim, S. Zhang, L. Zhang, Z. Xia, L. Dai, N. Park, J.-B. Baek, *Sci. Rep.* **2013**, *3*, 1810.

[17] G. Wu, N. H. Mack, W. Gao, S. Ma, R. Zhong, J. Han, J. K. Baldwin, P. Zelenay, *ACS Nano* **2012**, *6*, 9764–9776.

[18] a) C. Huang, C. Li, G. Shi, *Energy Environ. Sci.* **2012**, *5*, 8848–8868; b) L. Feng, Y. Yan, Y. Chen, L. Wang, *Energy Environ. Sci.* **2011**, *4*, 1892–1899; c) J. P. Paraknowitsch, A. Thomas, *Energy Environ. Sci.* **2013**, *6*, 2839–2855.

[19] a) T. Sharifi, G. Hu, X. Jia, T. Wågberg, *ACS Nano* **2012**, *6*, 8904–8912; b) Z.-H. Sheng, L. Shao, J.-J. Chen, W.-J. Bao, F.-B. Wang, X.-H. Xia, *ACS Nano* **2011**, *5*, 4350–4358.

[20] a) R. Cao, R. Thapa, H. Kim, X. Xu, M. Gyu Kim, Q. Li, N. Park, M. Liu, J. Cho, *Nat. Commun.* **2013**, *4*, 2076; b) Y. Liang, Y. Li, H. Wang, J. Zhou, J. Wang, T. Regier, H. Dai, *Nat. Mater.* **2011**, *10*, 780–786.

[21] a) H. Zhao, Y.-P. Zhu, Z.-Y. Yuan, *Eur. J. Inorg. Chem.* **2016**, 1916–1923; b) W. Xu, Z. Lu, P. Wan, Y. Kuang, X. Sun, *Small* **2016**, *12*, 2492–2498; c) J. Masa, P. Weide, D. Peeters, I. Sinev, W. Xia, Z. Sun, C. Somsen, M. Muhler, W. Schuhmann, *Adv. Energy Mater.* **2016**, *6*, 1502313.

Received: July 31, 2016